**Solution-processed flexible temperature sensor array for highly resolved spatial temperature and tactile mapping using ESN-based data interpolation**

*Haruki Nakamura[1,2†], Ryota Ezaki[2†], Guren Matsumura[2†], Chia-Chen Chung[3, 4], Yu-Chieh Hsu[3, 4], Yu-Ren Peng[3, 4], Akito Fukui[1], Yu-Lun Chueh[3,4, 5], Daisuke Kiriya[6], Kuniharu Takei[1]**

[1]Graduate School of Information Science and Technology, Hokkaido University, Sapporo 060-0814, Japan

[2]Department of Physics and Electronics, Osaka Metropolitan University, Sakai 599-8531, Japan

[3]Department of Materials Science and Engineering, National Tsing-Hua University, Hsinchu 30013, Taiwan

[4]College of Semiconductor Research, National Tsing-Hua University, Hsinchu, 30013, Taiwan

[5]Department of Materials Science and Engineering, Korea University, Seoul 02841, Republic of Korea

[6]Graduate School of Arts and Sciences, The University of Tokyo, Tokyo 153-8902, Japan

[†]These authors equally contributed.

*Corresponding author: takei@ist.hokudai.ac.jp

**Keywords:** flexible sensors, $V_2O_5$, nanowires, machine learning, data interpolation

## ABSTRACT

High-performance flexible temperature sensors are crucial in various technological applications, such as monitoring of environmental conditions and human healthcare. The ideal characteristics of these sensors for stable temperature monitoring include scalability, mechanical flexibility, and high sensitivity. Moreover, simplicity and low power consumption will be essential for temperature sensor arrays in future integrated systems. This study introduces a solution-based approach for creating a $V_2O_5$-nanowire-network temperature sensor on a flexible film. Through optimization of the fabrication conditions, the sensor exhibits remarkable performance, sustaining long-term stability (>110 h) with minimal hysteresis and excellent sensitivity (~−1.5%/°C). In addition, this study employs machine learning techniques for data interpolation among sensors, thereby enhancing the spatial resolution of temperature measurements and adding tactile mapping without increasing the sensor count. Introducing this methodology results in an improved understanding of temperature variations, advancing the capabilities of flexible-sensor arrays for various applications.

## INTRODUCTION

Sensors are pivotal in enhancing comfortable and convenient living conditions by detecting various environmental factors, including temperature, humidity, pressure, and pollutants. With current advances in artificial intelligence, collecting and processing data from numerous sensors using machine learning algorithms have emerged as a new approach for constructing smart well-being platforms.[1, 2] Mechanically flexible sensors facilitate development of advanced technological applications on nonplanar surfaces, such as monitoring changes in human body temperature using skin-mounted sensors.[3] Unlike conventional silicon-based electronics, the development of flexible sensors necessitates active materials that exhibit electrical changes against temperature, which can be applied to flexible substrates with good mechanical bending properties. Flexible sensors present substantial technological opportunities, such as monitoring temperature distribution over a large surface area through tape-like attachment of sensors to target objects.[4, 5] However, covering extended areas implies the requirement for numerous sensors, fueling the need for low-cost fabrication approaches, such as printing or transfer methods. To date, various cost-effective flexible temperature sensors have been reported in the literature that use metal-, semiconductor-, and composite-based material systems,[6-15] each with distinct characteristics in terms of long-term stability[8] and high sensitivity.[7, 14, 15] Graphene oxide mixed with poly(ethylene oxide) and polyvinylidene fluoride has been employed in sensing devices, exhibiting a high sensitivity of ~11.2%/°C.[14] Long-term stability was achieved by employing carbon nanotube and $SnO_2$ nanoparticles;[8] however, the sensitivity (~0.23%/°C) is sacrificed to realize high stability. In contrast, vanadium oxide–based sensors exhibit relatively high sensitivity (~2.2%/°C) and stability (~10 h).[7] Using this vanadium oxide for application with regard to flexible sensors is challenging due to its fabrication temperature, i.e., 500°C, which is unsustainable for conventional flexible substrates owing to their thermal budget. Furthermore, vanadium oxide nanowire (NW)–based sensors show relatively high sensitivity (~1%/°C) when formed at low temperatures on a flexible film; meanwhile, their long-term stability is not studied.[16] A detailed comparison of the performances to other materials is described in Table S1. Other reliable and practical temperature sensors are based on Si-based pn diodes. Owing to the mature Si-diode technology, such sensors are highly stable and exhibit large voltage change output as a function of temperature even after transferring the diode onto a flexible film.[17] However, the techniques used for transferring the diode from a wafer fabricated using a Si-based process to a flexible film increase the device's cost for macroscale-sensor-array application. Although achieving high stability and sensitivity is crucial for developing flexible temperature sensors, combining these features with mechanical flexibility at low fabrication costs remains challenging. Based on previous pioneering works, vanadium oxide–based materials are promising for fabricating high-performance, high-stability, flexible temperature sensors if the fabrication temperature can be reduced. In addition, low power consumption requirements mandate a high spatial temperature-distribution resolution using a minimal number of sensors, necessitating smart data processing approaches such as data interpolation between sensors.

This study presents the development of a solution-based temperature sensor using a $V_2O_5$-NW-network film (Figure 1a) to address the mentioned challenges. Although vanadium oxide has demonstrated potential for high-sensitivity temperature sensor applications,[6, 7, 18] achieving its long-term sensing performance stability through a solution-based macroscale process is yet to be realized. In this context, a $V_2O_5$-NW-network film is created through chemical bonding between the NW surface and target substrate, with screen-printed Ag electrodes serving as interconnections for the overall sensor. Good stability and high sensitivity are simultaneously realized by optimizing the fabrication process. Furthermore, a proof-of-concept cubic-structure device employs the developed flexible temperature sensors placed in contact on all sides of the cube (Figure 1b). Data collected from the six temperature sensors inside the cubic structure were processed through machine learning algorithm–based interpolation. This processing generates temperature and tactile maps, including locations such as corners without a sensor. Notably, the data interpolation approach proposed here to enhance the spatial temperature resolution and tactile mapping using flexible and printed temperature sensors has not been previously reported. The approach outlined herein combines long-term stability, relatively high stability, low hysteresis, and data interpolation to improve the spatial resolution of temperature distribution monitoring.

## RESULTS AND DISCUSSION

A solution of $V_2O_5$ NWs was synthesized following the method reported by Fukui et al.,[19] with detailed information on $V_2O_5$ NW synthesis and temperature sensor fabrication provided in Supporting Information (Figures S1 and S2). Atomic-force-microscopy imaging demonstrates the uniform formation of the $V_2O_5$ NW network on the film surface (Figure 1c). In addition, Figure 1d showcases the device's flexibility, highlighting its ability to be bent with no material delamination from the substrate.

The crystallinity of the $V_2O_5$ NW network was examined using X-ray diffraction (XRD) both before and after thermal annealing at 250°C for 30 min (Figure 2a). The XRD spectrum before annealing displays two peaks corresponding to the (111) and (710) orientations of the $V_2O_5$ NW network, consistent with the PDF-00-041-1426 phase of $V_2O_5$. Notably, the intensities of these peaks are heightened in the XRD spectrum after annealing, indicating an improvement in the crystallinity of the layers. Before annealing, transmission electron microscopy (TEM) images of the $V_2O_5$ NW network confirm its crystalline nature (Figures 2b–d). The TEM images presented in Figures 2e–g clearly illustrate the enhanced crystallinity of the $V_2O_5$ NW network after annealing. Moreover, the elemental composition of the $V_2O_5$ NW network was investigated using energy-dispersive X-ray spectroscopy (EDS), revealing consistently stable atomic concentrations of oxygen (before: 81.2% and after: 82.5%) and vanadium (before: 18.8% and after: 17.5%) before and after annealing (Table S2). In both cases, EDS mapping (Figure S3) identified a uniform distribution of oxygen and vanadium along the NWs. Although TEM and XRD investigations were employed herein, further systematic analyses are required to understand the material's change at different annealing conditions. As the present study aims to develop a stable temperature sensor and developed sensor–based application, a detailed investigation of the material outbounds the current scope and is planned for future studies.

Various samples were tested in different environments at variable annealing temperatures to investigate the sensor's hysteresis behavior and temperature sensitivity (temperature coefficient of resistance (TCR)). The design of the sensor is presented in Figure S4. Herein, the structural dependences, such as the involved electrode's distance and width, were not investigated. For scalability with better performance of the sensor, this design needs to be further optimized. Here, we focused on studying $V_2O_5$ NW network annealing to achieve a high TCR and stability. Nonannealed samples and those annealed under $N_2$ and forming gas ($H_2/N_2$) exhibited unstable performances (data are not shown). Therefore, performance investigations were conducted only for samples annealed under vacuum conditions. Under these conditions, the resistance across the $V_2O_5$ NW network was measured against temperature changes, revealing that the resistance decreases with increasing temperature (Figures 3a and b and S5). These observations align with a well-known sensing mechanism related to electron hopping conduction between $V^{5+}$ and $V^{4+}$ impurity centers.[6, 18] Figure 3c illustrates the linear relation between 1000/T and Ln ($T/R$), where $T$ denotes temperature and $R$ represents the sensor's resistance across the measured temperature range. This linearity corresponds to the electron hopping probability between the $V^{5+}$ and $V^{4+}$ impurity centers.[6]

Temperature sweeps (increasing and decreasing) were applied under different annealing conditions to examine the hysteresis behavior. The results indicate a decreasing tendency of hysteresis as the temperature increases. In particular, the sensors annealed at 250°C exhibit approximately zero hysteresis (Figure 3b). This observation is likely linked to the improved crystallinity of the $V_2O_5$ NW network at higher temperatures, as demonstrated by the TEM and XRD results, resulting in enhanced material stability. However, further investigations are needed to deepen the understanding of the stability mechanism, which is beyond the scope of this study. Using the sample annealed at 250°C, the sensor TCR was obtained as −1.5%/°C through linear fitting of $\Delta R/R_0$ versus temperature (Figure 3d), where $R_0$ is the initial resistance at T = 30°C and $\Delta R = R(T) - R_0$. In this case, TCR evaluation through linear fitting gives a rough estimation, given the sensing mechanism associated with the electron-hopping conductance change. Clearly, the hysteresis gradually decreases with increasing annealing temperature (Figures 3a and b and S5). Because of approximately zero hysteresis, the TCR difference (ΔS) between the increasing- and decreasing-temperature cases is small (approximately 0.024%/°C ± 0.001%/°C). By contrast, it is one order of magnitude larger (approximately 0.15%/°C ± 0.04%/°C) for the sample annealed at 100°C (Figure 3e). Notably, there is only small TCR variations (i.e., TCR ~ 1.31%/°C ± 0.20%/°C) between multiple samples (Figure S6).

To assess the sensor's performance on a flexible substrate, the impact of mechanical strain was investigated by measuring the resistance change ratio $\Delta R/R_0$ between flat and bent sensors. Figure 4a illustrates that the sensor resistance increases with decreasing bending radius, whereas the resistance change ratio against temperature, corresponding to TCR, remains approximately constant (Figure 4b). Although an exact measurement of the bending condition requires a strain sensor (not integrated in this study), the temperature can be readily calculated because of the constant TCR of the sensor.

The long-term reliability of the sensor was evaluated by subjecting it to repeated thermal-change cycles from 25°C to 60°C and vice versa for >110 h in an environment-controlled oven

(Figure 4c). In the initial 20 h, resistance values exhibited small (0.5%) increasing shifts at 25°C. However, the sensor stabilized after 20 h, exhibiting no observable resistance shifts. These results underscore the stability of the temperature sensor fabricated using an all-solution-based process. Next, the humidity response of the sensor was examined by changing both humidity and temperature. The resistance of the $V_2O_5$ NW network increases at high relative humidity (RH) when directly exposed to moisture (Figure S7). To suppress the effect of moisture on the sensor, the $V_2O_5$-NW-network film was laminated using a polyimide tape, resulting in a relatively stable output even under RH of 90% (Figure 4d). Notably, owing to the use of a polyimide tape over the sensor, water molecules can be diffused (especially at high RH of >80%) through the tape's glue, inducing a slight drift on the sensor output. Realizing good stability at different humidity condition requires a chemically bonded protection layer without any glue over the sensor to block water molecules.

Hereafter, the application of the developed flexible temperature sensor is described in conjunction with a data-interpolation machine learning algorithm for monitoring temperature and tactile mapping across large areas. This investigation aims to demonstrate the feasibility of mapping temperature and tactile distributions even in areas with no installed physical sensor, thereby achieving extensive sensing coverage with a reduced number of sensors. For this purpose, a cubic-structure device was fabricated using six integrated temperature sensors (one on each internal facet). The sensor outputs were measured using a data logger while the entire cubic structure, including its facets and corners, was heated to temperatures ranging from 60°C to 100°C. An echo state network (ESN),[20] a reservoir computing framework, was employed to predict the contact location and object temperature. ESN tunes only the weights of the output layer to obtain analysis results without tuning the weights of the input or internal layers, making it easy to analyze data with high accuracy in a short training time. The system was designed to simultaneously output locations and temperatures from only one reservoir with all sensor inputs on the cubic-structure device. Preprocessing and random forests,[21] which classify several states at the output layer, were introduced (Figure 5a). Two preprocessing steps were conducted as follows: first, outliers were removed by complementing the data with those before the outlier occurrence when the difference of sensor values from initial values was >100 kΩ. Second, the differential values of the data were extracted after processing the removal of the outliers, enabling the capture of a temperature change as a slope of the resistance change. During the measurement, objects heated to 60°C–100°C were in contact at four locations and resistance changes were recorded in three cycles conducted at each location. Two cycles were used as training data, and one cycle was used as test data for detection and evaluation. The cubic structure of the device and the resistance changes over time during the tests are presented in Figures 5b and c, respectively. Location and temperature predictions were conducted (Figures 5d and e). To identify the location, the response of each sensor was measured and classified into three categories. When two sensor outputs from the ESN are in the ON state, the system output is classified as "corner." If only one sensor output is ON, the output is classified as "plain," whereas if none of the sensor outputs is ON, the output is set to "none." Temperature detection was classified into 60°C, 70°C, 80°C, 90°C, and 100°C. The results show that the location and temperature detections are well predicted despite some observed spike noises. Recall was used as a parameter to quantitatively assess the system prediction accuracy:

$$Recall = \frac{TP}{TP+FN}, \qquad (1)$$

where TP and FN represent the numbers of true positives and false negatives, respectively. Precision is calculated using the following equation:

$$Precision = \frac{TP}{TP+FP}, \qquad (2)$$

where FP represents the number of false positives. When searching for the optimal hyperparameters in an ESN, the harmonic mean of Precision and Recall, denoted as the F1 score, is used. Given that temperature prediction involves a six-class classification, $F1_{temperature}$ is computed by considering the harmonic mean of the F1 scores obtained from all location predictions. Subsequently, $F1_{location}$ is calculated for each location prediction. Finally, $F1_{temperature\&location}$ is derived by taking a harmonic mean of $F1_{temperature}$ and $F1_{location}$. A grid search was employed to enhance the system accuracy, and the hyperparameters were determined based on the grid search results (Figure S8). A summary of the Recall values is presented in Figures 5f and g. Detection rates of >86% were achieved for both location and temperature, except for the 100°C detection, which achieved 70%. In the control analysis, detection accuracy was compared between cases with and without the second preprocessing step. The results reveal an overall improvement in the system accuracy with the entire preprocessing case (Figures 5f and g and S9). However, specific temperature predictions slightly improved in the case without second preprocessing. Further optimization of data processing and ESN hyperparameters may enhance this accuracy. Nevertheless, the present findings affirm the system's capability to accurately predict temperatures below 90°C using data interpolation. Linear interpolation or other methods can be alternatively employed for data processing. However, the use of the conventional interpolation method without machine learning requires the static state of temperature output. In this elastomer-based structure, it takes very long time to reach the static state of the temperature owing to the low thermal conductivity of the elastomers. To quickly analyze the sensor output, nonlinear outputs—which machine learning can be used to analyze—were utilized to estimate the temperature and location before reaching the temperature static state. Furthermore, memory is important to accurately estimate the output due to the nonlinear function of the temperature variation. To use the memory effect, ESN was examined, which exhibited more accurate outcomes compared to the estimation results without ESN (i.e. linear regression or random forests only) (Table S3). A detailed explanation regarding the mean squared error (MSE) for linear regression is described in Experimental Method. As proof of concept, images of the contact location of the object and its temperature were displayed by changing the images' colors and plotting the temperature value (Figure 5h). Although data interpolations were successfully examined, spatial and temperature resolutions could not be discussed, which are important parameters for sensor array applications. To confirm these resolutions, a further detailed study is required, which cannot be addressed here owing to equipment limitations.

Based on the results of the sensor and data analysis, the performance and functionality are discussed by comparing other previously reported temperature sensors (Table S1). Although the sensor reported herein does not exhibit the highest TCR compared to other solution- or transfer-based resistive temperature sensors, it achieves excellent total performance, including high TCR, negligible hysteresis, and long-term stability, which are the most important parameters for temperature sensors. Furthermore, as proof of concept, data interpolation—which could be used to realize long-term stability and negligible hysteresis—was demonstrated to achieve a high spatial temperature resolution with less number of sensors.

## CONCLUSIONS

This study demonstrates a cost-effective solution-based fabrication method for a long-term-stable, flexible temperature sensor with negligible hysteresis behavior. The fabricated temperature sensor exhibits long-term stability (>110 h) with negligible hysteresis and good TCR (~−1.5%/°C). In addition, the study incorporates data interpolation using an ESN to enhance the spatial resolution of temperature distribution without increasing the number of temperature sensors. A cubic-structure device equipped with six temperature sensors on its plane surface was employed to validate the effectiveness of data interpolation. As proof of concept, simultaneous detection of the tactile location and its temperature on both plane surfaces and corners of the cubic structure was successfully demonstrated. These results indicate that the combination of sensor arrays and data analysis using machine learning enables high-spatially-resolved temperature mapping with a minimal number of sensors. Practical applications, including wearable devices or internet of things–based devices, should be demonstrated by optimizing structures such as curved or spherical surfaces. As this study aims to demonstrate a high TCR of the long-term-stable flexible temperature sensor formed using an all-solution-based process and to propose using data interpolation to improve spatial resolution, practical applications are beyond its scope and need to be addressed in future works. Notably, data analyses differ depending on the device designs so that a new ESN algorithm is required to apply this data interpolation for different applications. Another target of this study is to realize a cost-effective sensor on a flexible film. The material cost is approximately US$0.02 per sensor, which can be further reduced during mass production. The approach presented herein provides a pathway to develop simpler and lower-power-consumption sensing systems compared to currently employed conventional methods.

## EXPERIMENTAL METHOD

**Synthesis of a $V_2O_5$ NW solution:** Ammonium metavanadate, an acidic ion-exchange resin, and deionized (DI) water were mixed in a ratio of 1:10:100.[19] Ammonium metavanadate was first added to DI water. After stirring the solution, the acidic ion-exchange resin was added (Figure S1a). The prepared solution was mixed on a hot plate set at 60°C for 20 min and shaken using a shaker at room temperature for one week. After shaking, 20% of the top surface of the liquid was extracted (Figure S1b). This solution contained $V_2O_5$ NWs; it was then placed in a centrifuge set at 12,000 rpm for 4 h. The top layer of the solution (Figure S1c) was extracted to obtain high-purity $V_2O_5$ NWs.

**Fabrication process of the temperature sensor:** Process schematic is presented in Figure S2. $SiO_x$ with a thickness of 10 nm was deposited on a 125-μm PI film using an electron-beam evaporator. The $SiO_x$ surface was treated using oxygen plasma; then, poly-L-lysine was drop-casted onto the surface for 10 min. Subsequently, poly-L-lysine was washed and dried through air blow. This surface modification led to the formation of a uniform and high-density $V_2O_5$ NW network on $SiO_x$. On the chemically modified $SiO_x$ surface, the $V_2O_5$ NW solution was drop-casted and kept for 30 min to form $V_2O_5$ NW networks. Finally, silver electrodes were formed using a screen printer for interconnection of the sensors, and a PI film was laminated over the temperature sensor to protect it from humidity and mechanical scratches.

**Definition of MSE:** MSE was used to evaluate the system, especially considering linear regression. MSE was calculated as follows:

$$\mathrm{MSE} = \frac{1}{N} \sum_{i=1}^{N} (y_i - \hat{y}_i)^2, \qquad (3)$$

where $y_i$ represents the actual value of the target, $\hat{y}_i$ is the value estimated using machine learning, and $N$ represents the number of datasets. A small MSE value indicates that the target is estimated well.

## ASSOCIATED CONTENT

**Supporting Information**. Supporting Information is available free of charge at.

Fabrication process, TEM and EDS mapping of $V_2O_5$ NWs, device design, hysteresis behavior, TCR variation, humidity response of the sensor without a protection layer, grid search results of the ESN, confusion matrix without the second preprocessing step, performance comparison with other studies, atomic concentrations before and after annealing, and accuracy comparison between the cases of with and without the ESN.

## AUTHOR INFORMATION

**Corresponding Author**

*E-mail: takei@ist.hokudai.ac.jp

**Author Contributions**

K. T. conceived the concept; H. N., R. E., G. M., and K. T. designed the research and experiments; H. N and R. E. performed the experiments and analysis on all device sections; C.-C. C., Y.-C. H., Y.-R. P., and Y.-L. C. performed XRD and TEM analyses; G. M. performed all ESN developments; and A. F. and D. K. performed $V_2O_5$ NW synthesis. All authors contributed to discussions, providing insights, analysis, and manuscript writing. †These authors contributed equally.

**Notes**

The authors declare no competing financial interest.

## ACKNOWLEDGMENT

This work was partially supported by the JST AIP Accelerated Program (Grant No. JPMJCR21U1), JSPS KAKENHI (Grant No. JP22H00594), JST ALCA-Next (Grant No. JPMJAN23F2), the Murata Science Foundation, the Hitachi Global Foundation, and the Takeda Science Foundation.

## ABBREVIATIONS

EDS, energy-dispersive X-ray spectroscopy; ESN, echo state network; MSE, mean squared error; RH, relative humidity; TCR, temperature coefficient of resistance; TEM, transmission electron microscopy; XRD, X-ray diffraction.

## REFERENCES

(1) Ballard, Z.; Brown, C.; Madni, A. M.; Ozcan, A. Machine Learning and Computation–Enabled Intelligent Sensor Design. *Nat. Machine Intell.* **2021**, *3*, 556–565.

(2) Ha, N.; Xu, K.; Ren, G.; Mitchell, A.; Ou, J. Z. Machine Learning-Enabled Smart Sensor Systems. *Adv. Intell. Syst.* **2020**, *2*, 2000063.

(3) Madhvapathy, S. R.; Arafa, H. M.; Patel, M.; Winograd, J.; Kong, J.; Zhu, J.; Xu, S.; Rogers, J. A. Advanced Thermal Sensing Techniques for Characterizing the Physical Properties of Skin. *Appl. Phys. Rev.* **2022**, *9*, 041307.

(4) Luo, Y.; Abidian, M. R.; Ahn, J. H.; Akinwande, D.; Andrews, A. M.; Antonietti, M.; Bao, Z.; Berggren, M.; Berkey, C. A.; Bettinger, C. J.; et al. Technology Roadmap for Flexible Sensors. *ACS Nano* **2023**, *17*, 5211–5295.

(5) Xu, K.; Lu, Y.; Takei, K. Flexible Hybrid Sensor Systems with Feedback Functions. *Adv. Funct. Mater.* **2021**, *31*, 2007436.

(6) Muster, J.; Kim, G. T.; Krstić, V.; Park, J. G.; Park, Y. W.; Roth, S.; Burghard, M. Electrical Transport Through Individual Vanadium Pentoxide Nanowires. *Adv. Mater.* **2000**, *12*, 420–424.

(7) Liao, F.; Zhu, Z.; Yan, Z.; Yao, G.; Huang, Z.; Gao, M.; Pan, T.; Zhang, Y.; Li, Q.; Feng, X.; Lin, Y. Ultrafast Response Flexible Breath Sensor Based on Vanadium Dioxide. *J Breath Res.* **2017**, *11*, 036002.

(8) Yamaguchi, T.; Kashiwagi, T.; Arie, T.; Akita, S.; Takei, K. Human-Like Electronic Skin-Integrated Soft Robotic Hand. *Adv. Intell. Syst.* **2019**, *1*, 1900018.

(9) Yang, Y.; Song, Y.; Bo, X.; Min, J.; Pak, O. S.; Zhu, L.; Wang, M.; Tu, J.; Kogan, A.; Zhang, H.; et al. A Laser-Engraved Wearable Sensor for Sensitive Detection of Uric Acid and Tyrosine in Sweat. *Nat. Biotech.* **2019**, *38*, 217–224.

(10) Zhang, M.; Sun, J. J.; Khatib, M.; Lin, Z. Y.; Chen, Z. H.; Saliba, W.; Gharra, A.; Horev, Y. D.; Kloper, V.; Milyutin, Y.; et al. Time-Space-Resolved Origami Hierarchical Electronics for Ultrasensitive Detection of Physical and Chemical Stimuli. *Nat. Commun.* **2019**, *10*, 1120.

(11) Xu, Y.; Zhao, G.; Zhu, L.; Fei, Q.; Zhang, Z.; Chen, Z.; An, F.; Chen, Y.; Ling, Y.; Guo, P.; et al. Pencil-Paper On-Skin Electronics. *Proc. Natl. Acad. Sci. U.S.A.* **2020**, *117*, 18292–18301.

(12) Lee, J.; Chen, H.; Kim, E.; Zhang, H.; Wu, K. T.; Zhang, H.; Shen, X. P.; Zheng, Q.; Yang, J.; Jeon, S.; Kim, J.-K. Flexible Temperature Sensors Made of Aligned Electrospun Carbon Nanofiber Films With Outstanding Sensitivity and Selectivity Towards Temperature. *Mater. Horiz.* **2021**, *8*, 1488–1498.

(13) Daus, A.; Jaikissoon, M.; Khan, A. I.; Kumar, A.; Grady, R. W.; Saraswat, K. C.; Pop, E. Fast-Response Flexible Temperature Sensors with Atomically Thin Molybdenum Disulfide. *Nano Lett.* **2022**, *22*, 6135–6140.

(14) Lee, Y.; Park, J.; Choe, A.; Shin, Y. E.; Kim, J.; Myoung, J.; Lee, S.; Lee, Y.; Kim, Y. K.; Yi, S. W.; et al. Flexible Pyroresistive Graphene Composites for Artificial Thermosensation Differentiating Materials and Solvent Types. *ACS Nano* **2022**, *16*, 1208–1219.

(15) Shin, Y.; Kim, Y. W.; Kang, H. J.; Lee, J. H.; Byun, J. E.; Yang, J. Y.; Lee, J. W. Stretchable and Skin-Mountable Temperature Sensor Array Using Reduction-Controlled Graphene Oxide for Dermatological Thermography. *Nano Lett.* **2023**, *23*, 5391–5398.

(16) Neto, J.; Dahiya, A. S.; Dahiya, R. Influence of Printed Encapsulation Layer on the Mechanical Reliability and Performance of V2O5 Nanowires-Based Flexible Temperature Sensors. In IEEE J. Flexible Elecron., 2023.

(17) Kim, D. H.; Wang, S.; Keum, H.; Ghaffari, R.; Kim, Y. S.; Tao, H.; Panilaitis, B.; Li, M.; Kang, Z.; Omenetto, F.; et al. Thin, Flexible Sensors and Actuators as 'Instrumented' Surgical Sutures for Targeted Wound Monitoring and Therapy. *Small* **2012**, *8*, 3263–3268.

(18) Adbel-Latif, R. M. DC Electrical Measurements on Evaporated Thin FIlms of Vanadium Pentoxide. *Physica B* **1998**, *254*, 273–276.

(19) Fukui, A.; Aoki, Y.; Matsuyama, K.; Ichimiya, H.; Nouchi, R.; Takei, K.; Ashida, A.; Yoshimura, T.; Fujimura, N.; Kiriya, D. Single-Layered Assembly of Vanadium Pentoxide Nanowires on Graphene for Nanowire-Based Lithography Technique. *Nanotechnology* **2021**, *33*, 075602.

(20) Nakajima, K.; Fischer, I. Reservoir Computing; Theory, Physical Implementation, and Applications. *Springer Nature* **2021**.

(21) Breiman, L. Random Forests. *Machine Learning* **2001**, *45*, 5–32.

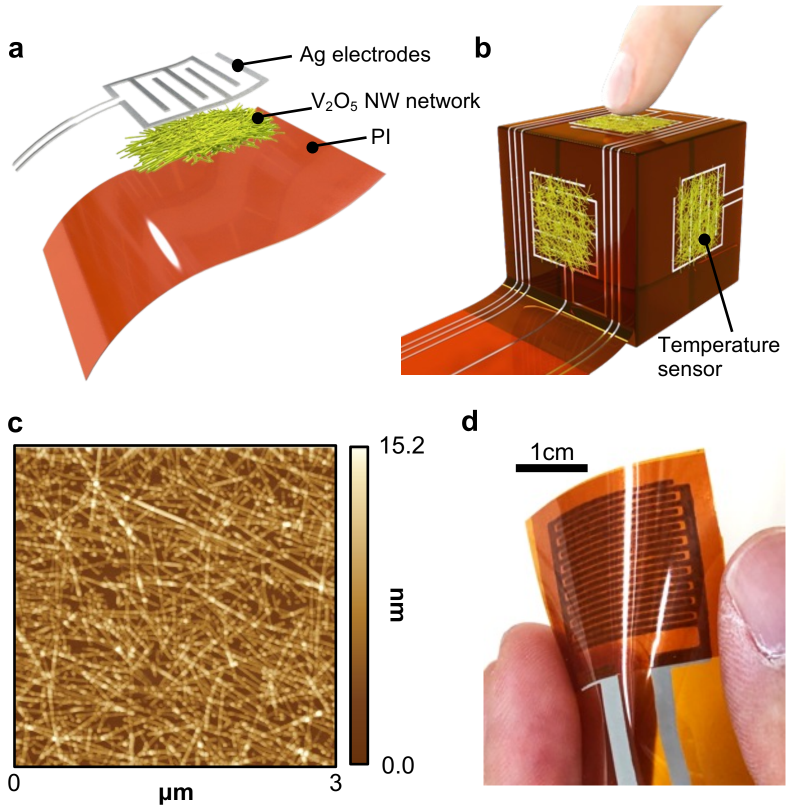


**Figure 1.** Schematics of (a) the temperature sensor structure and (b) a cubic-structure device integrated with six temperature sensors. (c) AFM image of the $V_2O_5$ nanowire network. (d) Photograph of the fabricated flexible temperature sensor.

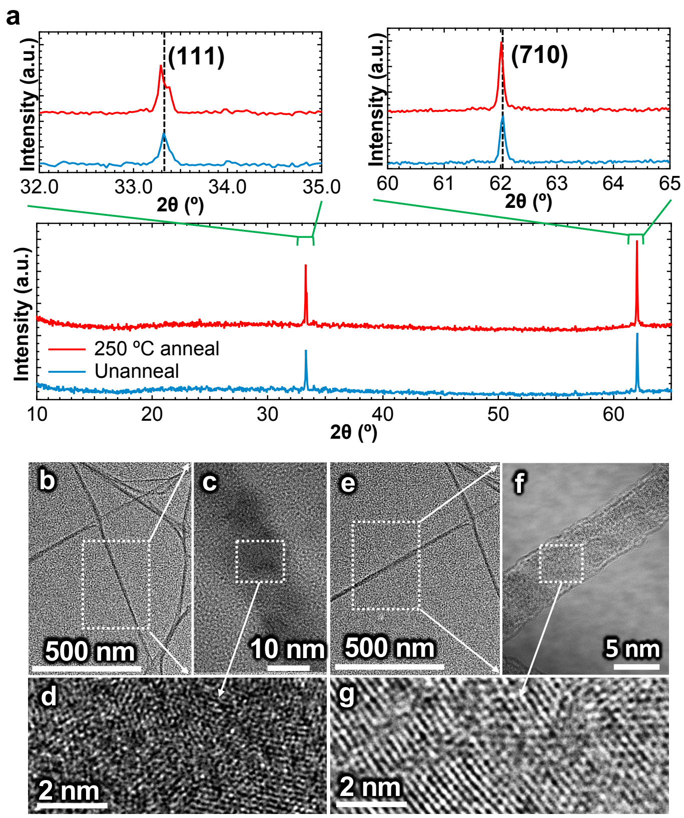


**Figure 2.** Material characterizations of $V_2O_5$ NWs before and after thermal annealing. (a) XRD spectra and TEM images of $V_2O_5$ NWs (b)–(d) before and (e)–(f) after annealing. (d)(g) Corresponding high-resolution TEM images.

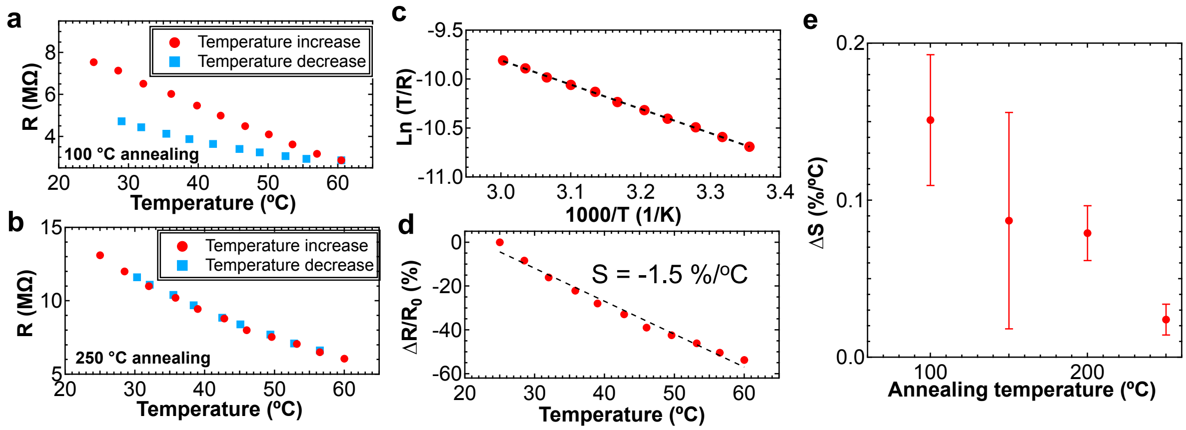


**Figure 3.** Sensor resistance as a function of temperature for (a) 100°C annealing and (b) 250°C annealing. (c) Temperature dependence of the sensor for electron hopping conductance. (d) Resistance change ratio of the sensor at different temperatures to obtain the TCR. (e) TCR difference between the cases of increasing and decreasing temperatures for hysteresis discussion.

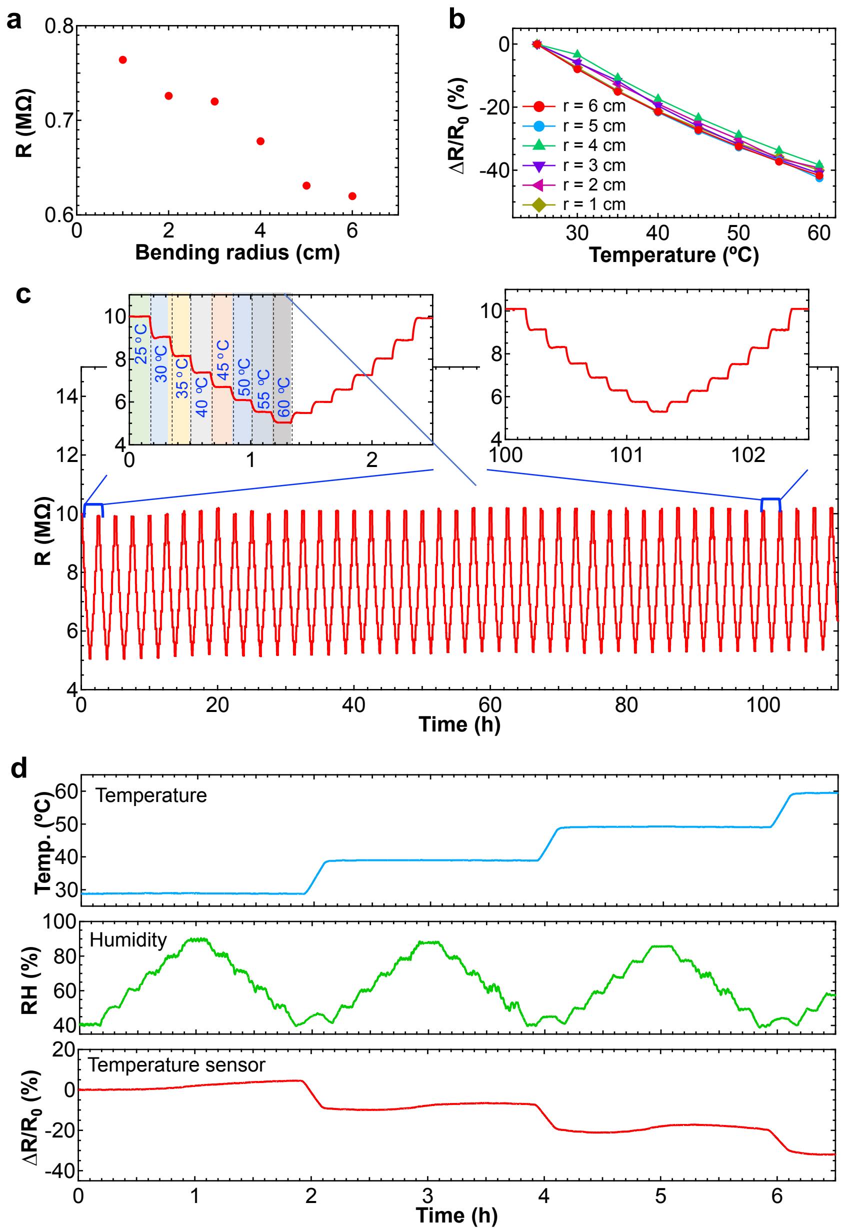


**Figure 4.** (a) Resistance of the sensor as a function of the bending radius. (b) Resistance change ratio at different temperatures and bending radii. (c) Cycle test at temperatures ranging from 25°C to 60°C for 110 h. (d) Real-time sensor response at different humidities and temperatures.

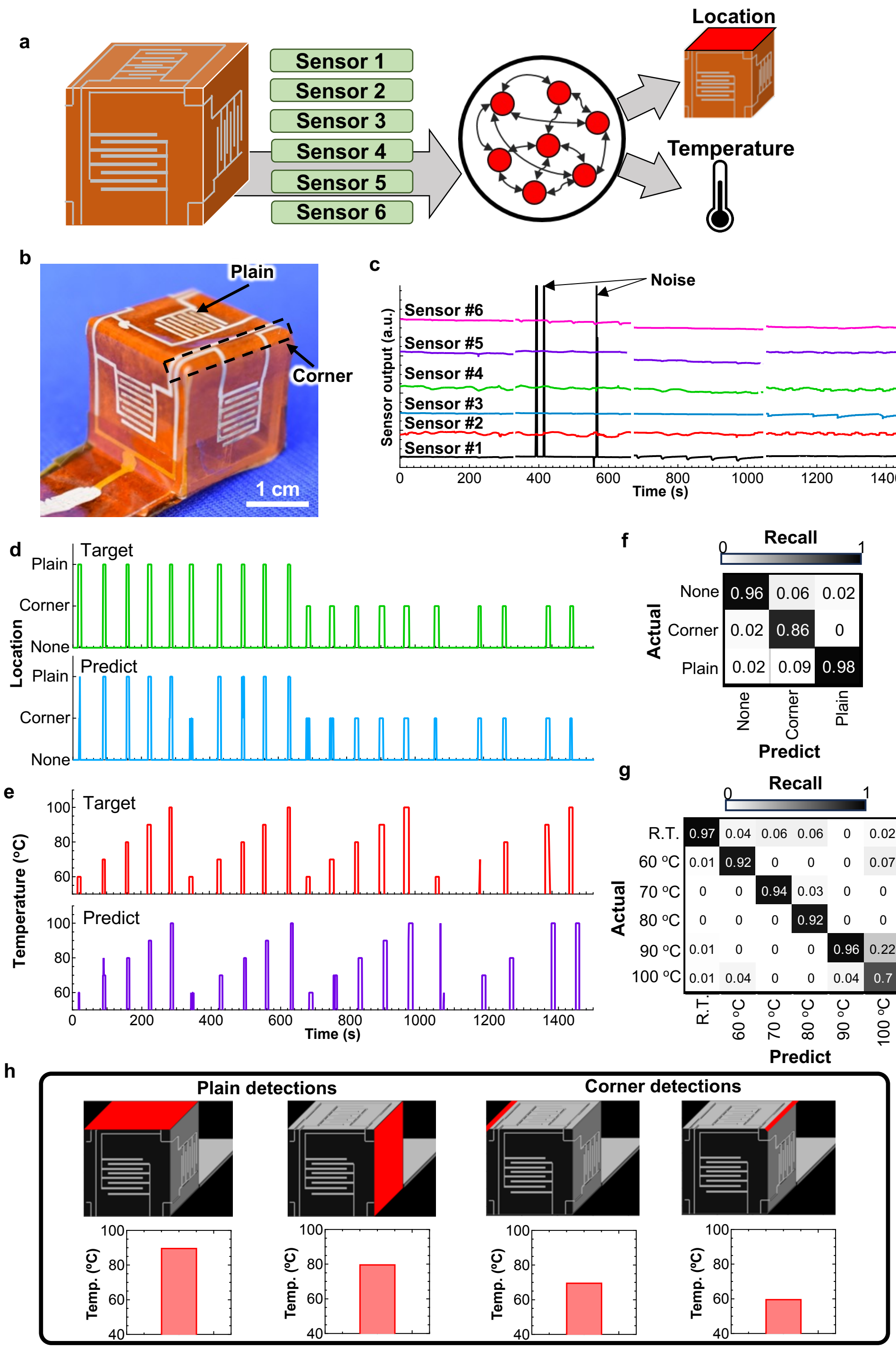


**Figure 5.** (a) Process of the multitasking ESN to obtain location and temperature predictions. (b) Photograph of the cubic-structure device integrated with six temperature sensors. (c) Sensor outputs to predict the touching location and temperature using the ESN. Target and predicted

outputs of (d) locations (plain, corner, and none) and (e) temperatures from 60°C to 100°C. Confusion matrices of (f) location and (g) temperature detections. (h) Visible-output demonstration of the touching location and object temperature. A red plane or line on a cubic-structure image indicates the location of touch.

## Table of Contents